Materials Today Sustainability 21 (2023) 100334

Contents lists available at ScienceDirect

Materials Today Sustainability

journal homepage: https://www.journals.elsevier.com/materials-today-sustainability

Chitosan-hydroxyapatite composites made from sustainable sources: A morphology and antibacterial study

F. Scalera [a], S.I.A. Pereira [b], A. Bucciarelli [a, c], D.M. Tobaldi [a], A. Quarta [a], F. Gervaso [a], P.M.L. Castro [b], A. Polini [a], C. Piccirillo [a, *]

[a] CNR NANOTEC, Institute of Nanotechnology, Campus Ecoteckne, Lecce, Italy
[b] Universidade Católica Portuguesa, CBQF – Centro de Biotecnologia e Química Fina – Laboratório Associado, Escola Superior de Biotecnologia, Porto, Portugal
[c] Laboratorio RAMSES, IRCCS Istituto Ortoperico Rizzzoli, Bologna, Italy

ARTICLE INFO

Article history:
Received 16 June 2022
Accepted 14 January 2023
Available online 21 January 2023

Keywords:
Cork
Natural template
Sustainable material
Biomedicine
Antibacterial activity

ABSTRACT

Chitosan (Cs) and hydroxyapatite (HA) 3D scaffolds/composites were prepared with a sustainable process, as HA was obtained using $CaCO_3$ derived from cork, a natural material used as a template agent. The HA@Cs composites were prepared with HA in situ formation in a Cs solution, with a dissolution-precipitation mechanism.

Different reaction times were considered, with time of 72 h leading to the best materials (sample CsHA_72). X-ray Diffraction (XRD) analysis confirmed HA formation. The analysis of Cs unit cell parameters showed that, for the unmodified Cs, the cell had larger dimensions and a higher degree of distortion than previously reported in literature; HA incorporation in the CsHA_72 composite led to a further increase in the cell dimensions.

The morphology of the scaffolds was studied with Scanning Electron Microscopy (SEM) and a high level of porosity was observed; a statistical comparison was performed between the unmodified Cs and CsHA_72 to determine the pore size, structure, and distribution. This analysis, the first of this kind for this type of composites, showed smaller and more circular pores for the CsHA_72 composite (average diameter of 70 μm vs. 88 μm for unmodified Cs). The overall level of porosity, however, did not change (>77%); likewise, the Young modulus was not affected by HA incorporation (about 11 kPa).

Antibacterial tests, performed on *Escherichia coli* and *Staphylococcus aureus*, showed that HA presence did not significantly reduce the antimicrobial properties; the composites were particularly effective towards *S. aureus*, as a >90% the bacterial population reduction was observed for an incubation time of 2 h. HA@Cs also showed excellent biocompatibility and good cell proliferation.

The properties of these 3D scaffolds make them suitable for application as biomaterials.

1. Introduction

The development of sustainable processes for the preparation of materials and devices is a fundamental challenge of our society today; there is in fact an increasing demand due to higher world population and industrialisation, which cannot be achieved with the traditional processes. This is due to both the availability of the raw materials and the impact some processes have on the environment [1,2]. Within this frame, the reuse and valorisation of by-products/residues of industrial processes can reduce the use of raw material and, hence, have a beneficial effect on the environment [3].

Chitosan (Cs) is a natural polysaccharide, with functional properties that make it suitable for different technological applications; it is, in fact, highly biocompatible and biodegradable. Moreover, it shows antibacterial properties and good cell-adhesive properties; for all these features it is used for biomedical applications [4,5]. In addition to this, Cs can be employed in the food and cosmetic industry [6]. Cs is derived from chitin, a compound which is extracted from the shells of crustaceous, such as shrimps, i.e. residues of the fish processing industry; it is therefore a material produced according to the principles of the circular economy [7].

Further than the valorisation of industrial residues, the use of natural compounds as template agents is another way to make synthesis and manufacturing more sustainable. In traditional processes, in fact, template agents are synthetic and, hence, prepared

* Corresponding author.
E-mail address: clara.piccirillo@nanotec.cnr.it (C. Piccirillo).

https://doi.org/10.1016/j.mtsust.2023.100334
2589-2347/

through reactions using chemicals; to manufacture 3D porous scaffolds for biomedicine, for instance, synthetic polymers such as polyurethane are often used as template agents [8]. Their substitution with natural materials would reduce the impact on the environment. Natural compounds often have a particular morphology, which can impart improved properties to the materials; indeed, literature reports on different ceramic 3D structures made using wood as template agents [9].

Cork is the bark of the *Quercus suber* L. tree; its structure consists in cells, which are arranged in a hexagonal honeycomb and in a rectangular shape in the radial and transverse directions, respectively [10]; their average dimensions are 40–45 and 15–20 μm. Cork is a very sustainable material as the tree is not cut when the bark is harvested (every 9–13 years); furthermore, to grow the cork back the tree absorbs CO_2, promoting a beneficial impact on the environment. Due to these features and to its sustainability cork has been used as template agent to prepare different ceramic compounds, including ferrites and calcium carbonate [10,11]; in all cases the prepared materials kept the same 3D cork structure. Considering in particular $CaCO_3$, subsequently it was converted into hydroxyapatite [12].

Hydroxyapatite (HA, $Ca_{10}(PO_4)_6(OH)_2$) is a calcium phosphate widely used in biomedicine. HA is in fact the main component of the human bone; it is very biocompatible and osteoconductive (i.e. capable of inducing bone formation [13]). Because of this, HA is employed to fabricate bone substitute, to replace damaged bones due to diseases or traumas [14]. Unmodified HA, however, does not have antibacterial properties; because of this, infections can develop in HA-based bone implants [15]. A way to avoid this is to combine HA with other materials possessing antibacterial behaviour; the composites should maintain HA osteoconductive activity and, at the same time, inhibit bacterial growth.

Composites made of Cs and HA were developed and studied with this objective; indeed, literature reports of enhanced cellular growth [16], combined with antibacterial behaviour [17,18]. The performances of such composites can be affected by several parameters, including their morphology, porosity [19] as well as a uniform intermixing between the two phases [20].

In the present work we report about sustainable HA@Cs composites in form of 3D scaffolds where HA was prepared using $CaCO_3$ derived from cork; different experimental conditions were tested to obtain the composites with best properties. These materials were characterised in terms of composition; their morphology was studied with Scanning Electron Microscopy (SEM) methodology, and pore structure and distribution were analysed statistically. Porosity and mechanical behaviour were also investigated. Moreover, the antibacterial activity and biocompatibility were also tested.

2. Materials and methods

2.1. Preparation of the composites

HA@Cs composites were prepared by *in situ* HA formation in a chitosan solution. For the HA to be formed, $CaCO_3$ derived from cork was used as starting material; the process has been previously described in literature [11], a brief summary is reported here. Cork powder (30–50 μm dimension) was pyrolysed to obtain graphitic carbon; successively, it was infiltrated with a calcium source (calcium acetate) and then pyrolysed again, to form $CaCO_3$.

To prepare the composite: a chitosan solution (2% w/v, low Molecular Weight, Sigma Aldrich) was prepared in 1% v/v acetic acid and stirred until complete solubilisation at room temperature. The cork-derived $CaCO_3$, prepared as described above, was used for the synthesis. A 10 mM suspension was prepared; successively, a $(NH_4)_2PO_4$ solution (6 mM in acetic acid 1% wt/v, pH = 5.5) was added drop by drop.

The obtained suspension was stirred at room temperature for different lengths of time – 24, 48 or 72 h. After this time, the slurries were poured into petri dishes and freeze dried for 24 h. The obtained samples were then ionically cross-linked to obtain a more stable 3D structure by placing them in a mixing of NaOH and Na_2SO_4, in a ratio of 1:4 (1 and 0.5 M, respectively) for 48 h. Crosslinked scaffolds were washed in distilled water twice to remove the excess of the reagents and then were freeze dried for 24 h.

Selected samples were calcined at 700 °C, with a ramp of 5 °C/min and a dwell time of 1 h.

2.2. Chemical-physical characterisation

The phase composition of the composite was determined by X-Ray Diffraction (XRD) with an X' Pert PRO MRD diffractometer, equipped with a fast RTMS detector, using a CuKα radiation (40 kV and 40 mA). Data were recorded in the 20–80 °2θ range, with a virtual step-scan of 0.02 °2θ, and virtual time-per-step of 200 s. The whole powder pattern modelling (WPPM) method [21], as implemented in the PM2K software suite [22], was used to determine the unit cell parameters of prepared specimens. With this method each observed peak profile is considered as a convolution of instrumental and sample-related physical effects; the corresponding model parameters are directly refined on the observed data [23]. To this aim, the instrumental contribution was obtained and taken into account in the modelling, by fitting nine *hkl* reflections from the NIST SRM 660b standard (LaB_6), according to the Caglioti relationship [24]. Monoclinic unit cell of chitosan, described in the space group $P2_1$ was taken from the literature [25]. The parameters refined in the WPPM modelling were the background (modelled using an 8th-order Chebyshev polynomial function), peak intensities, specimen displacement, and unit cell parameters.

Thermogravimetric analysis was performed on the scaffolds to determine the amount of HAp formed during the reaction using a SDT Q600 apparatus (TA Instruments). Samples were analysed by Scanning Electron Microscopy (SEM) with a Sigma Instrument. Before the analysis samples were sputtered with gold.

A statistical analysis was performed on some selected SEM images, following a previously developed protocol [26], to study the pores structure and distribution of the composite samples in comparison with the unmodified chitosan. The micrographs (100× magnification V=5 kV, W_d=4.4 mm) were thresholded using the percentile method and segmented to individuate the pores; from this, the pores area A and their dimeter D was extrapolated, and then the equivalent diameter D was calculated using the circular approximation (see equation (1)).

$$D = 2^{*}\sqrt{\frac{A}{\pi}} \tag{1}$$

From this, the circularity C and the aspect ratio AR were calculated, according to equations (2) and (3) respectively.

$$C = \frac{4\pi^{*}A}{P^2} \tag{2}$$

$$AR = \frac{l_{MAX}}{l_{MIN}} \tag{3}$$

The circularity C is the degree to which the particle is similar to a circle, taking into consideration the smoothness of the perimeter; this means circularity is a measurement of both the particle form and roughness. Consequently, the less the particle is perfectly

round, the lower the *C* value becomes. The aspect ratio *AR*, on the other hand, describes how elongated the particle is, considering the maximum distance and the minimum distance of two points on the perimeter (also referred to as Feret maximum and minimum distance l_{MAX} and l_{MIN}, respectively).

The distributions for all these quantities were compared using the non-parametric Mann–Whitney *U* test, with the confidence levels were assigned as follows: $p \leq 0.1$ (.), $p \leq 0.05$ (*), $p \leq 0.01$ (**), $p \leq 0.001$ (***).

The porosity of the scaffolds was determined following a previously reported protocol [27]. The scaffolds were placed into an excess of dry ethanol for 30 min; their weight was measured before and after the immersion. The porosity (%) was calculated according to formula (4):

$$P\ (\%) = \frac{W_f - W_i}{\rho V} * 100 \quad (4)$$

where W_f and W_i are the weight after and before the immersion, r is the density of ethanol and V is the volume of the scaffold. Five tests were performed for each sample; the calculated value was an average, with the associated standard deviation.

The mechanical properties of the scaffolds were measured with uniaxial compression tests, in displacement control, up to 75% of the strain. Samples with dimensions of 6 mm in diameter and 3 mm in thickness were used, at a rate of 0.01 mm/s and with a load cell of 10 N. Four replicates for each scaffold were tested in wet conditions. From the stress strain correlation the Young modulus was calculated, in the linear region of the curve (strain range 0–10%).

2.3. Antibacterial activity

The antibacterial activity of HA@Cs composites was tested with the viable cell count method, with a previously used protocol [27] with some modifications.

The strains were grown in Mueller Hinton Agar medium at 37 °C overnight. From the freshly grown cultures, liquid inocula were prepared in an isotonic solution (NaCl 0.85%) with a concentration of about 10^8 CFU/mL 300 μL of liquid culture were placed into each well of 12 multi-well plate containing 2.7 mL of sterile saline solution and the HA@Cs scaffolds. The composites were previously sterilized with UV light irradiation, for 10 min on each side.

The samples were left in contact with the liquid inocula under gentle stirring (80–90 rpm). At selected times (1, 2 and 5 h), aliquots were taken from the plates and appropriately diluted using 0.85% NaCl sterile solution. The diluted solutions were plated on Plate Counting Agar (PCA) medium and incubated at 37 °C for 24–48 h; then the number of the grown colonies were counted.

Two strains were tested, a Gram-positive and a Gram-negative, *Staphylococcus aureus* ATCC 6538 and *Escherichia coli* ATCC 25922, respectively.

Control experiments were performed using bacterial inocula only (no sample) and unmodified Cs scaffolds.

2.4. Cytotoxicity and cell proliferation

The cytotoxicity of the sample was assessed with the Trypan Blue exclusion assay. Human osteosarcoma cells, namely MG63 (ATCC Manassas, Virginia, USA) were cultured in high glucose Dulbecco's Modified Eagle Medium (DMEM) supplemented with 10% Fetal Bovine Serum (FBS), 100 U/mL penicillin and 100 μg/mL streptomycin at 37 °C in an atmosphere of 5% CO_2. Disks of either Cs or CsHA_72 (around 1 cm diameter) were prepared, washed with sterile phosphate buffer saline (PBS), sterilized under the UV light for 2 h and placed into each well of 24-well culture plates. Then 5×10^4 cells dispersed in 1 mL of culture medium were seeded into each well. Cells seeded directly into the multiwells were used as control samples (CTRL). After 1, 3 and 7 days incubation cells were trypsinized and counted in a Burker chamber by using standard trypan blue method. The percentage of viable cells was estimated according to formula (4):

$$Viability\ (\%) = \frac{Number\ of\ viable\ cells}{Number\ of\ total\ cells} * 100 \quad (4a)$$

Cell proliferation was determined with MTT assay. Discs of **Cs** and **CsHA_72**, prepared like described above, were placed into 24-well culture plates. Then, 5×10^4 cells dispersed in 1 mL of culture medium were seeded into each well. At 1, 3 and 7 days after seeding the medium was removed from the plates and the samples were washed twice with PBS The MTT reagent (3-(4,5-dimethylthiazol-2-yl)-2,5-diphenyl tetrazolium bromide) was dissolved into culture medium without serum (final concentration 2 mg/mL). Then, 1 mL of the medium was added to each plate and incubated for 2 h at 37 °C. Subsequently it was removed, and the dark-blue formazan crystals produced by MTT metabolisation were solubilized by dimethyl sulfoxide. Finally, the absorbance of the obtained solutions was measured using the CLARIO star Plus microplate reader (BMG Labtech, Germany), ($\lambda = 570$ nm). The assay was also performed on blank film samples (i.e. **Cs** and **CsHA_72** samples without cells) to assess any colorimetric interference. For each sample, an average value from 3 independent replicates was calculated.

In addition to this, fluorescence imaging was also performed. MG63 cells were seeded into each well of a 24-well culture plate containing the samples. After 3 and 7 days, the medium was removed, the cells washed with PBS and fixed paraformaldehyde (4% in PBS). Then, 500 μL of (1:10,000 v/v) DAPI solution in PBS was added to each well and incubated at r.t. in the dark for 20 min to stain the nucleus. Afterwards, the samples were washed with PBS and 400 μL of phalloidin-TRITC solution (5 μg/mL) was added to each well, incubating for 40 min h in the dark at room temperature. Finally, the samples were washed with PBS prior to be imaged under Fluorescence Microscope EVOS m7000 (ThermoFisher, Waltham, MA, USA).

3. Results

3.1. Characterisation of the scaffold

As stated in the previous section, HA was prepared *in situ* by reaction between the cork-derived $CaCO_3$ and a phosphorus source. The concentration of the powder suspended into the Cs solution was 20 times lower than that of the Cs itself; this was done because with an excessive powder loading the viscosity of the solution would have became too high, hindering the reaction and limiting the porosity of the freezedried composite. It has to be reminded, however, that a certain ratio between Cs and HA in solution may correspond to different proportions in the solid final material [28]. Different reaction times were considered, to see the effect on the HA formation – 24, 48 and 72 h, corresponding to the samples **CsHA_24**, **CsHA_48** and **CsHA_72** respectively. A relatively long cross-linking time was considered (48 h); indeed it was observed that shorter times were not sufficient for the HA to precipitate.

Fig. 1(a) shows the TGA curves for the three scaffolds, while in Fig. 1(b) the first derivative of the curves are reported. The behaviour of the composites is compared to that of unmodified **Cs** (data already published [29]). As previously reported, **Cs** is completely degraded at about 500 °C; in fact no residual weight is present at higher temperatures. The main weight loss can be registered for

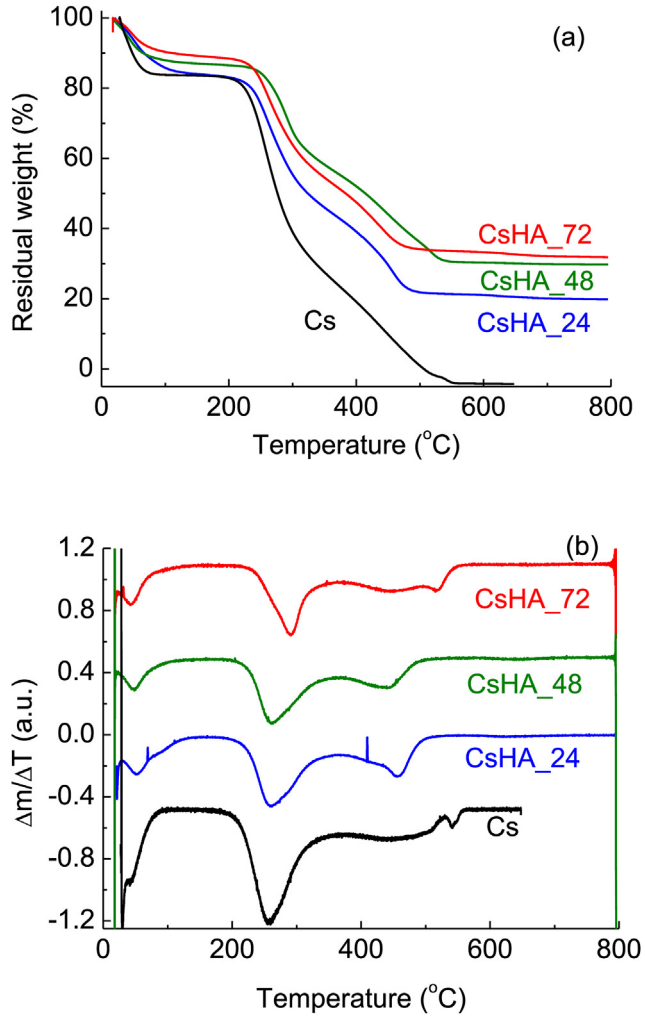

Fig. 1. TGA data for CsHA composites prepared for different lengths of time; (a) TGA curves, (b) first derivatives of the curves.

150 < T < 500 °C, when the chemical bonds of the polymeric matrix get degraded. For the composites, on the other hand, it can be seen that there is some residual weight, different according to the reaction time; this corresponds to the inorganic phase present in the composites. The data are summarised in Table 1; an increase in the residual weight can be observed with longer reaction times – about 19, 30 and 32% for 24, 48 and 72 h respectively.

The first derivative curves show that the main peak is for 150 < T < 400 °C, as observed for the unmodified **Cs**; there is, however, a slight shift to higher temperatures – from about 255 °C for **Cs** to about 293 °C for **CsHA_72**; this indicates that a higher proportion of the mineral phase corresponds to an increased thermal stability. This is in agreement with literature data [30]; indeed the mineral phase can behave as a thermal barrier and delay the decomposition. Moreover, chitosan thermal stability can also be affected by the level of cross-linking which, in turn, can be affected by the presence of other phases in its network [31]. At higher temperatures an additional peak can be observed for 400 < T < 600 °C; the shape and the intensity of the peak are different according to the reaction time. It is interesting to note, however, that the weight change was registered for T > 600 °C, indicating that $CaCO_3$ is not present in significant concentration in the composite; it is known, in fact, that a de-carboxylation takes place for 600 < T < 800 °C [32].

Table 1
Residual weight (%) after TGA treatment at 800 °C.

Sample	Residual weight (%)
CsHA_24	19.8
CsHA_48	29.7
CsHA_72	32.0

To determine the phase composition of the scaffolds, XRD analysis were performed; the diffraction patterns of the composites are shown in Fig. 2. It can be seen that the most intense peak for the chitosan phase detected in the **Cs** sample is for 2θ = 25.5°. Compared this value with what reported in literature, lower diffraction angles were generally observed [33,34], although some studies with higher angles' value can also be found [35]. Such differences can be due to distortion in the structure and/or lattice dimensions, which in turn can be affected by the kind and extent of cross-linking [33]. For the composites, the same chitosan peak was shifted to slightly lower diffraction angles, indicating an increase in the unit cell dimensions. This point will be discussed more in detail later.

Regarding HA presence, its most intense peak at 2θ = 31.7° (JCPDF file 01-072-1234) is not visible in the **CsHA_24** sample; it is very weak for **CsHA_48** and more well defined for **CsHA_72**. HA peak is not very sharp but, on the contrary, it is quite broad; this is reasonable, since the reaction was performed at room temperature (to avoid any damage to the Cs network) and hence HA has very low crystallinity. This can explain why the signal is not detected for samples **CsHA_24** and **CsHA_48** despite the relatively high weight concentration (about 19 and 30 wt %, see Table 1). It is interesting to note that no peak corresponding to the original $CaCO_3$, is detected, in agreement with TGA data.

To verify that the formed mineral phase was HA, with no other phosphates present, the composite samples were calcined at 700 °C. As shown by the TGA data, Cs was completely degraded at this temperature and the only residue is the mineral part; XRD data of these residues were acquired – see Figure SI1 for the results. All peaks match the HA diffraction pattern, and no peak for β-TCP is detected (2θ = 31.0°); this confirmed that the reaction led to the formation of HA only, with no other phases – a result which was expected, as a stoichiometric ratio of 1.67 was used between Ca and P. A very weak peak is present at 2θ = 37.3°, which corresponds to CaO (JCPDF file 00-37-1497); this may be due to very small quantity of unreacted $CaCO_3$ which turns into CaO.

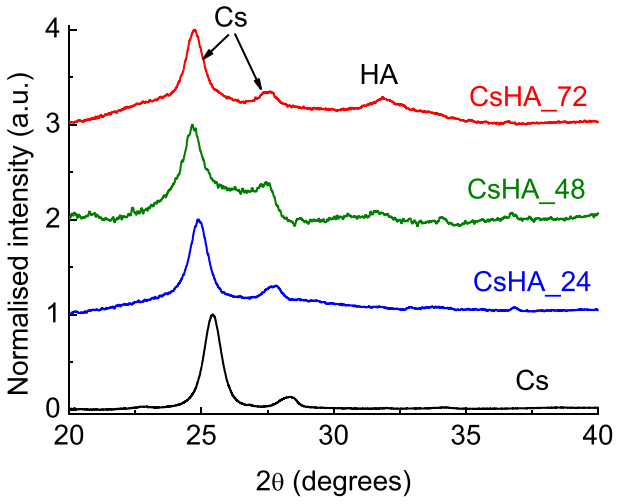

Fig. 2. XRD patterns for single-phase Cs sample and composite CsHA samples prepared for different lengths of time.

Based on the XRD results of the composites, it was concluded that sample **CsHA_72** was the one with the best characteristics, due to higher HA content; therefore, further tests and analysis were performed.

More XRD studies were carried out to determine the effects of the HA presence on the chitosan unit cell parameters, as a shift in the position of the peaks were observed. To this aim, XRD data were analysed by means of WPPM method, see Table 2; an example of the WPPM output is displayed in Figure SI2. Considering the unmodified **Cs** sample, it is interesting to see that both cell dimensions and interaxial angle beta are greater than reported in literature [25]; this confirms that, according to the preparation protocol and cross-linking method, the characteristics of the polymer can be different. Comparing **Cs** to **CsHA_72**, a clear expansion in the unit cell parameters and volume is registered; the interaxial angle beta, on the other hand, did not change significantly. Such increase could be due to a partial diffusion of Ca^{2+} and/or $(PO_4)^{3-}$ ions into Cs network, as previously reported in literature [36]; other investigations instead report of a partial HA incorporation into the Cs structure [37]. It is likely that both process occur for **CsHA_72** sample.

Fig. 3 reports SEM images for samples **Cs** (a) and **CsHA_72** (b), which show a significant difference in their morphoplogy; despite both samples having a pore-based structure, in fact, pores are much smaller for the HA-containing composite. This indicates that HA formation led to a decrease in the average pore size; this effect was observed also for the samples prepared for 24 and 48 h (Figure SI3 (a) and (b) respectively). Indeed SEM images show pores size becoming smaller for longer reaction times. In Fig. 3(c) and (d) images of the **CsHA_72** with higher magnifications are reported; some crystallites can be observed, confirming the uniform HA distribution within the Cs matrix. The crystallites have a slightly elongated shape and with an average length of 200−300 nm; their shape is different from those formed when this $CaCO_3$ precursor was used in a simple aqueous solution [12]. This is reasonable, since the reaction medium can have a significant effect on the morphology of the reaction products [38,39]. HA crystallites on the surface of Cs network were reported in other studies; again, their morphology can be different according to the preparation conditions [40].

A more detailed study on the pores distribution of the two scaffolds was performed, results are reported in Fig. 4 while the calculated data are in Table 3. Fig. 4(a) and (b) show the SEM images already employed in Fig. 3(a) and (b) with the corresponding segmentation; from these images, the average values of the pores diameter and area were calculated. It can be seen that the presence of HA within the chitosan matrix led to a material with smaller pores; in fact the mean value for the area was 5672 μm^2 for **CsHA_72** (vs. 8911 μm^2 for **Cs**), while the average diameter was 70 μm for **CsHA_72** (vs. 88 μm for **Cs**). The distribution of the values for the area and the diameter was also calculated − see the boxplots of the distributions in Fig. 4(c) and (d), respectively. Both distributions were skewed towards low values, although there were differences between the two samples, as **Cs** distribution resulted to be slightly more centred than the **CsHA_72**; for the area, in fact, the skewness was 4.5 and 7.5 for **Cs** and **CsHA_72**, respectively, while for the diameter the values were 1.8 and 2.7. This led to a less pronounced distribution tail, as shown by the lower kurtosis value for **Cs** sample compared to the composite (31.8 vs. 77).

In the diagram, the boxes showing 25 and 75% data thresold (Q1 and Q3 respectively) are also included; their length represents the interquartile range (50% of the data is inside this range). It can be seen that, for both area and diameter, the boxes of the **CsHA_72** sample resulted smaller than those of **Cs**, indicating a narrower distribution. The same trend was observed for the values of the standard deviation and IQR (see Table 3), both a measure of the dispersion of the distribution. This confirms that the distribution for sample **CsHA_72** is less spread than for **Cs**.

To assess whether HA presence affected the pore morphology, two shape factors were investigated − the circularity (which indicates how close the pore shape is to a circle, including its roughness) and the aspect ratio (which indicates if the shape is elongated toward an axis). They are shown in Fig. 4(e) (circularity) and 4(f) (aspect ratio); pores of sample **CsHA_72** are more circular and less elongated than those of **Cs**, as both values are smaller (see Table 3). Regarding data distribution, for circularity the distribution resulted well centred for both samples, while for the aspect ratio data were skewed towards lower ratio. It has to be highlighted that data of the distribution for area, diameter and aspect ratio were fitted by a log-normal function, while for the circularity a normal function was the most appropriate; these fittings are shown on the graphs. All the distributions were significantly different.

The porosity of **Cs** and **CsHA_72** function was also measured and the results are reported in Table 4. It can be seen that both samples show a high and comparable degree of porosity, just below 80%.

Generally it can be stated that HA presence led to significant changes both in the crystallographic dimensions of the unit cell, and in the pore dimensions and distribution, while the overall porosity of the scaffold did not change significantly.

Table 4 also shows the values of the Young modulus for both the samples; it can be seen that there is no significant difference between the two values, which are both around 11 kPa. This result is in agreement with the scaffolds having comparable porosity. Indeed, the similar beahviour of **Cs** and **CsHA_72** can also be seen from the stress-strain curves (Figure SI4) which are almost superimposable.

3.2. Antibacterial activity of the scaffolds

Fig. 5 shows the results of the tests for the antibacterial activity of the scaffolds **Cs** and **CsHA_72**, towards the Gram-negative and Gram-positive strains *E. coli* and *S. aureus*, Fig. 5(a) and (b), respectively. Control experiments were also performed. For *E. coli*, the bacterial viability decreases progressively with longer contact times, reaching a value of less than 50% of the initial population after 5 h; no significant decrease, on the other hand, was observed for the control (i.e. bacteria not in contact with any sample). No significant difference was registered between the single phase Cs sample and the HA@Cs composite one.

For *S. aureus*, a different behaviour of bacterial viability with time was observed. There was a decrease for the first 2 h, while for longer times the cells' viability increased again; this trend was

Table 2
WPPM agreement factors, unit cell parameters and unit cell volume of for samples **Cs** and **CsHA_72**.

Sample	Agreement factors			Unit cell parameters				
	R_{wp} (%)	R_{exp} (%)	χ^2	*a* (nm)	*b* (nm)	*c* (nm)	β (°)	V (nm^3)
Cs	6.09	5.93	1.03	0.9787(3)	1.0024(3)	1.0761(1)	106.0(1)	1.015(1)
CsHA_72	6.05	5.37	1.13	0.9826(1)	1.0205(1)	1.0868(1)	106.1(1)	1.047(1)

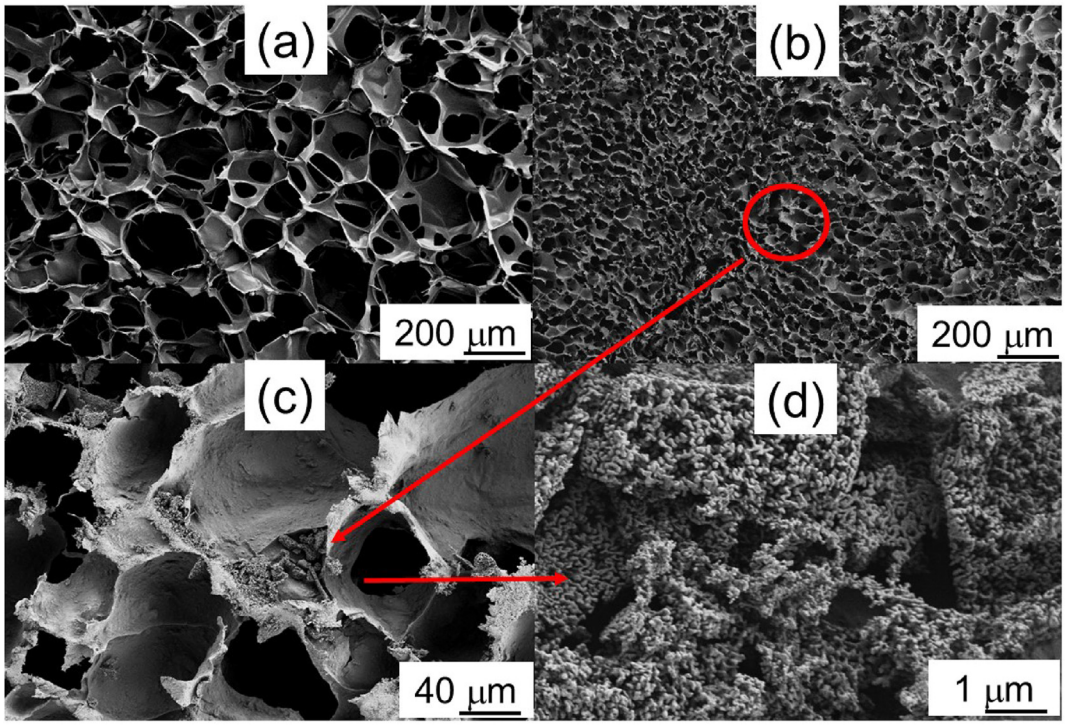

Fig. 3. SEM images of (a) **Cs** sample, (b) **CsHA_72** sample, (c and d) **CsHA_72** sample with higher magnification.

observed for both samples even if significant differences were observed between **Cs** and **CsHA_72**. In fact, after 1 and 2 h times, the bacterial activity was slightly higher for the **Cs** sample; **CsHA_72**, however, showed a deactivation higher than 90% for 2 h, indicating that the composite material is quite effective toward the Gram-positive strain. The increase in the bacterial viability observed for longer time indicates a regrowth of the microorganism, and it was previously reported for Cs-based antibacterial coatings [27]. Based on these results, it can be stated that composite sample **CsHA_72** are effective towards both Gram-positive and negative strains.

3.3. Cytotoxicity and cell proliferation

MG63 cells, a model of human osteosarcoma, were employed to assess the cytocompatibility of both unmodified Cs and HA@Cs composites; indeed such property is an essential requisite for any biomedical application [41]. Fig. 6 shows the results of the Trypan Blue assay; it can be seen that both scaffolds display optimal cell viability, with values higher than 80% for all time points (1, 3 and 7 days). Moreover, no significant difference can be observed between the two scaffolds and the control sample (cells seeded directly into the cell plate), nor between **Cs** and **CsHA_72**. The comparable behaviour between the two scaffolds could also be seen in the proliferation assay data (Figure SI5); both samples, in fact, show good proliferation profile, with a similar increasing trend in the studied interval (up to 7 days).

Fluorescent imaging of the cells grown on the scaffolds was performed, see Figure SI6. Indeed, for both **Cs** and **CsHA_72** a uniform cell distribution can be observed. Despite the fluorescence background of chitosan in the fluorescence window of DAPI, the nuclei and the cytoskeleton of the cells (stained with DAPI and Phalloidin-TRITC, respectively) can be detected, showing that the cells are layed on the walls of the polymer architecture. These results indicate the suitability for the prepared HA@Cs scaffolds for biomedicine use.

4. Discussion

Composites made of HA and a biopolymer with the phosphate formed *in situ* were previously reported in literature [28,42], although they constitute a minority. The majority of composites, in fact, are made using powdery HA already prepared, ideally nano-sized one. The advantage of *in situ* formation is that a more uniform distribution of the powder within the polymeric matrix can be achieved; moreover, changing the reaction conditions and/or reactants, the shape and size of the particles can be tailored [43]. Indeed literature reports of nano-HA formed *in situ* within a polymeric matrixes showing different morphologies (i.e. plate-like or more rounded shape) [42,44].

In this work, cork-derived $CaCO_3$ powder was employed as calcium source; such material showed a hierarchical porosity, as it resembled the original structure of the cork [11]. This feature allowed a good and uniform distribution of the reaction solution within its structure, maximising the contact with both Cs and the phosphorus source, hence leading to HA formation and its uniform distribution within the Cs matrix. The extent of the reaction depends on the time the process is carried out for; as the Cs solution is more viscous [45], it is reasonable to assume that the reaction is slower than in a simple aqueous medium.

No $CaCO_3$ signal was detected in the XRD patterns (Fig. 2); as reported in previous work, the cork-derived powder showed a remarkable level of crystallinity, with very sharp peaks [11]. These peaks would be visible even if a very small amount of $CaCO_3$ was present; their absence indicates that no residual carbonate is present in the composite. Our hypothesis is that the carbonate gets dissolved in the acid Cs solution and then a solution reaction between Ca and P takes place, to form HA which precipitates – i.e. a dissolution-precipitation mechanism. SEM micrographs of the

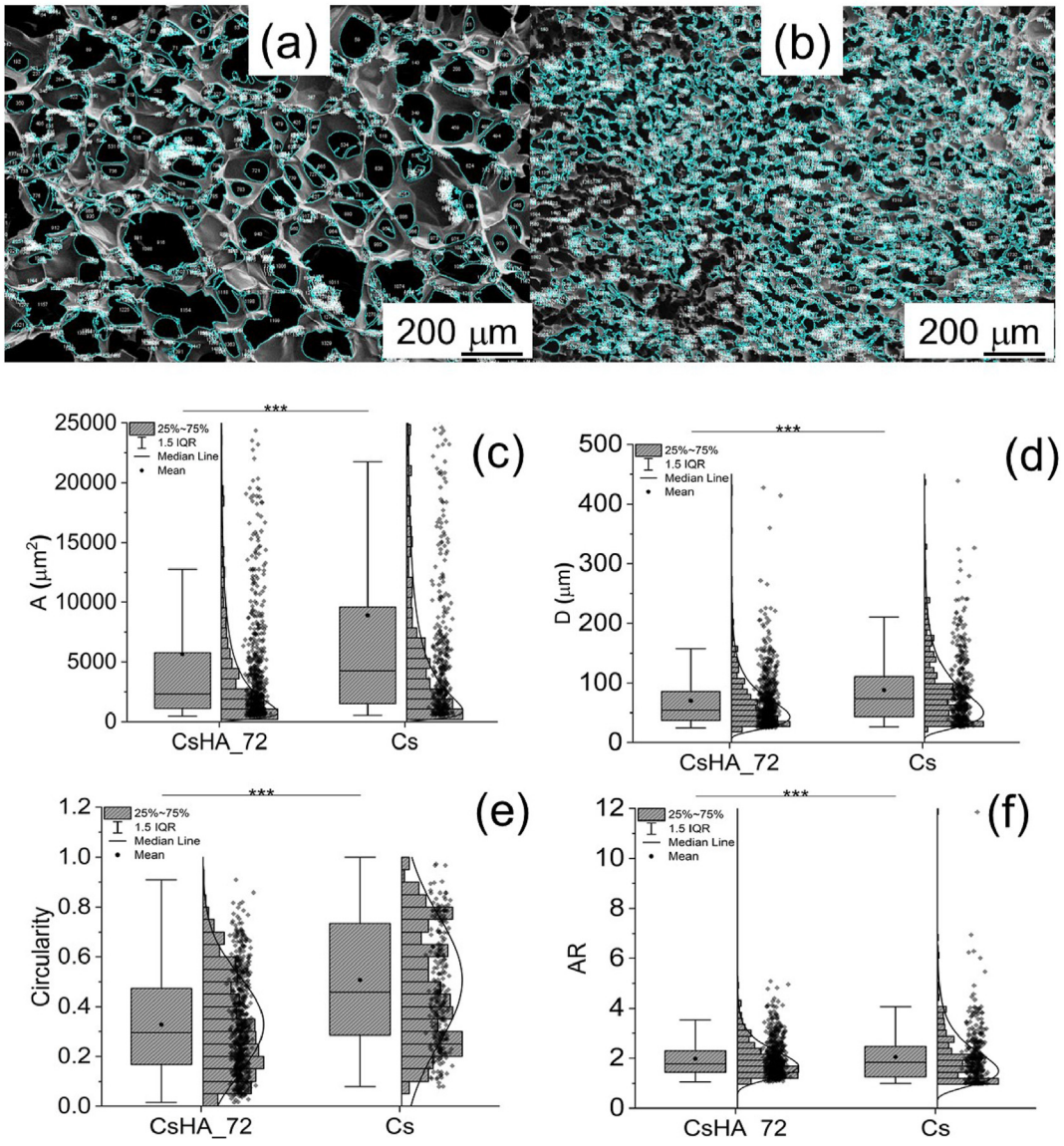

Fig. 4. Segmented SEM images for samples (a) **Cs** and (b) **CsHA_72**; Boxplots and distribution of pores (c) area, (d) equivalent diameter, (e) circularity and (f) aspect ratio.

Table 3
Descriptive statistic of the Area (A, μm^2), Diameter (D, μm), Circularity (C) and Aspect Ratio (AR) distributions of the single-phase **Cs** scaffold and the **CsHA_72** composite. The reported quantity are the mean value with the associated standard deviation, the skewness and kurtosis of the distribution, the minimum, maximum and median values, as well as those corresponding to Q1 and Q3.

	Mean	StD	Skew	Kurt	Min	Q1	Median	Q3	Max	IQR
$\mathbf{A_{CS}}$	8911.41	14199.54	4.53	31.81	543.74	1498.76	4245.34	9613.00	151172.98	8114.24
$\mathbf{A_{CsHA\_72}}$	5672.12	11184.63	7.50	76.96	483.74	1100.14	2316.61	5777.90	143397.34	4677.77
$\mathbf{D_{Cs}}$	88.25	59.73	1.79	4.53	26.31	43.68	73.52	110.63	438.72	66.95
$\mathbf{D_{CsHA\_72}}$	70.09	48.10	2.66	12.04	24.82	37.43	54.31	85.77	427.29	48.34
$\mathbf{C_{Cs}}$	0.47	0.23	0.31	−1.02	0.08	0.28	0.43	0.65	0.97	0.37
$\mathbf{C_{CsHA\_72}}$	0.33	0.19	0.52	−0.63	0.02	0.17	0.29	0.47	0.91	0.31
$\mathbf{AR_{Cs}}$	2.27	1.12	3.26	20.20	1.03	1.55	2.00	2.65	11.85	1.09
$\mathbf{AR_{CsHA\_72}}$	1.98	0.72	1.40	2.01	1.06	1.45	1.77	2.30	5.09	0.86

Table 4
Porosity (%) and Young modulus (kPa) for samples **Cs** and **CsHA_72**.

Sample	Porosity (%)	Young modulus (kPa)
Cs	77.5 ± 5.0	11.08 ± 1.36
CsHA_72	79.1 ± 10.1	11.78 ± 0.22

formed HA powder (Fig. 3(d)) show that the mineral does not maintain the honeycomb structure typical of the cork; this is in agreement with a dissolution of the solid powdery reactant.

SEM micrographs indicated that both the unmodified **Cs** and the composite **CsHA_72** scaffolds have a highly porous structure; this is in agreement with the high porosity measured for both samples

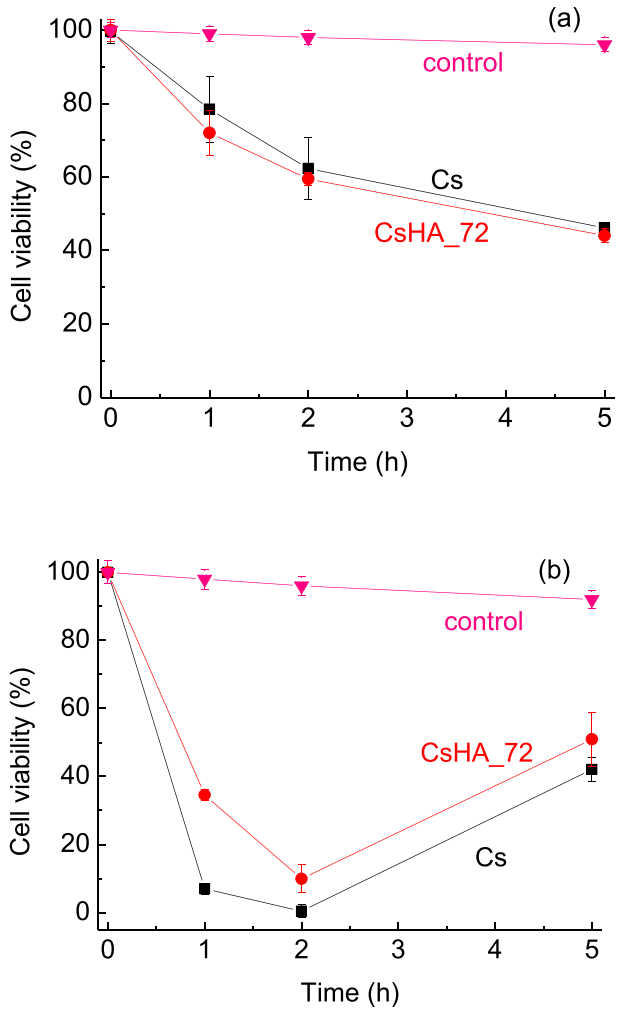

Fig. 5. Cell viability (%) for (a) *E. coli* and (b) *S. aureus* bacterial strains in contact with **Cs** and **CsHA_72** samples; control experiments are also reported.

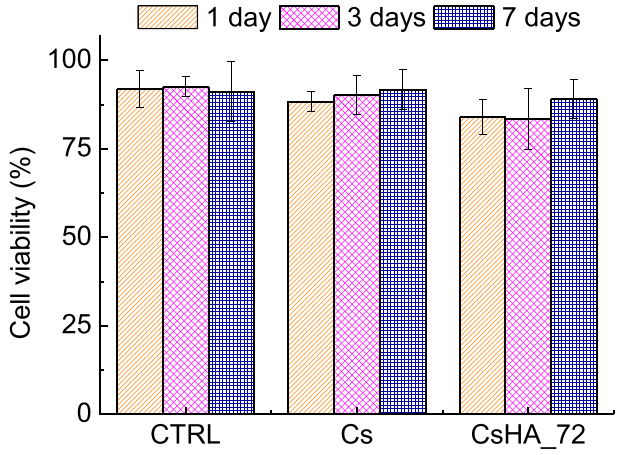

Fig. 6. Cell viability assay performed through Trypan blue exclusion assay after 1, 3 and 7 days incubation of MG63 cells with samples **Cs** and **CsHA_72**.

(see Table 4). A high level of porosity is a key element for a 3D scaffold; highly porous structures, in fact, favour cell adhesion and promote their proliferation. This, in turn, leads to improved growth of new bone [46]. The porosity of the scaffolds is affected by many parameters, such as the nature of the compounds scaffolds are made of and the protocol used in their preparation. In the specific case of Cs-based scaffolds, the protocol employed for the cross-linking as well as the cross-linking degree have a significant effect on porosity [47]. Moreover, the freeze-drying process, used for the scaffolds preparation, allows to have a high porosity value, which results from the sublimation of the ice crystals formed during the freezing step. As reported in previous studies, different dried freezing rates combined with cross-linkng allow a modulation of the pore size in polymers [48].

Despite the comparable levels of overall porosity, the statistical analysis of pores size and distribution of the two samples showed that HA formation and inclusion in the Cs matrix had a significant effect.

To our best knowledge, the methodology of statistical analysis by image segmentation applied here was reported in literature for other materials [26,49] but never applied in the specific case of Cs and its composites. Compared to other methodologies, the one employed here is based entirely on algorithms, thus excluding human bias and avoiding the counting of thousands of pores; this makes the statistical comparison between the different samples more reliable.

Previous studies on pore size distribution on freeze-dried Cs-based scaffolds were performed with different techniques, such as manual determination and microtomography [50,51]. Despite the use of different methodolgies, some comparison can still be made. Literature, in fact, reports of Cs-based scaffolds with pores of different dimensions; average values from 16 to 190 μm were observed [50,51], i.e. much lower and higher than those measured in this study (88 μm). Different level of skwness were also reported. These difference should not be seen as an inconsistency; it is known, in fact, that the pore distribution strongly depends on different parameters, including the methodology and extent of cross-linking, as well as the freeze-drying conditions. In this work, for instance, two bases (Na_2SO_4 and NaOH) were employed for the cross-linking; it is likely that their synergistic stabilising effect could have led to pores with dimensions which are different than previously reported [52].

The tests of the antibacterial activity of the composite sample **CsHA_72** confirm that Cs antimicrobial behaviour is maintained even when HA is present in its structure; this is in agreement with literature [18,28]. Compared to other published studies, the antibacterial activity of the Cs-based samples shown here is slightly lower. This could be explained considering the cross-linked structure of the composites prepared here; as reported in the previous sections, in fact, such composites have been cross-linked using a basic solution, which interacted with the aminic groups, leading to their deprotonation and/or formation of bonds with the ions of the solutions (SO_4^{2-} and OH). Such deprotonation may lead to a reduced antibacterial activity; according to literature, in fact, the positively charged amine groups of Cs backbone interact with the negative charges of microbial cell membrane. Consequently the membrane gets broken and this eventually leads to the death of the microorganisms [53,54]. Indeed literature reports on the effect that the neutralisation has on the antibacterial activity and how such effect can be different towards Gram-positive or −negative strains [55].

In our work, the antibacterial activity was more enhanced on the Gram-positive *S. aureus*; according to literature, the effectiveness towards this kind of strains can be affected by different parameters, including the molecular weight and the deacetylation degree [56]. Due to the difference in the time response between the 2 bacteria, the use of these samples in biomedicine is advisable for shorter time for Gram-positive microorganisms and longer one for Gram-negative ones.

Literature reports that adding HA into a Cs matrix improves the stability of the scaffolds [57]; although tests were not performed in this work, it is reasonable to assume that similar behaviour would be observed. Previous work performed by the authors, in fact, showed that 3D Cs-based scaffold prepared with the same protocol had increased stability after an inorganic phase was included in their structure [29].

It can be concluded that 3D composites with regular morphology and interesting functional properties can be made with Cs and cork-derived HA; due to their good biocompatibility they are suitable for biomedicine.

5. Conclusions

Sustainable HA@Cs composites were successfully prepared, with *in situ* HA formation using a $CaCO_3$ powder derived from cork. Due to $CaCO_3$ hierarchical porosity, a uniform distribution of the formed HA within the Cs matrix was obtained. XRD analysis of the composites showed that HA presence led to an increase in the dimensions of Cs crystallographic cell. SEM analysis showed the porous morphology of the scaffolds; from a study on pore dimension and distribution, significant differences were observed between the unmodified Cs and the HA@Cs composite, despite the overall level of porosity being comparable. Samples showed antibacterial properties, especially towards Gram-positive strains. Cell viability tests indicated the composites are not cytotxic and hence suitable as biomaterials.

As future work, further studies should be done on these materials; in particular, the ability of HA@Cs to induce cell differentiation into osteblast should be tested, for the composites to be used as effective antibacterial bone replacement materials.

Credit author statement

Clara Piccirillo, Francesca Scalera and Alessandro Polini designed the experiments and planned the work; Sofia Pereira and Paula Castro did the antibacterial tests; Francesca Scalera did the SEM analysis while Alessio Bucciarelli performed the segmented analysis; Clara Piccirillo performed the TGA and XRD data while David Tobaldi performed the XRD calculation and porosity tests; Francesca Gervaso did the mechanical tests while Alessandra Quarta performed the cellular studies. All authors contributed to the discussion and interpretation of the data, and the writing of the text.

Declaration of competing interest

The authors declare that they have no known competing financial interests or personal relationships that could have appeared to influence the work reported in this paper.

Ackowledgements

Clara Piccirillo and Francesca Scalera would like to thank Fondazione con Il sud for supporting this work (project HApECOrk, 2015–0243). Alessandro Polini, Francesca Gervaso and Alessio Bucciarelli are grateful to the “Tecnopolo per la medicina di precisione” (TecnoMed Puglia) - Regione Puglia: DGR n.2117 del 21/11/2018, CUP: B84I18000540002 and “Tecnopolo di Nanotecnologia e Fotonica per la medicina di precisione” (TECNOMED) - FISR/MIUR-CNR: delibera CIPE n.3449 del 7-08-2017, CUP: B83B17000010001. David Tobaldi was funded by EleGanTe – PON ARS01_01007. Paula Castro and Sofia Pereira thank Fundação para Ciência e Tecnologia for supporting this work (National Funds, project UIDB/50016/2020).

Appendix A. Supplementary data

Supplementary data to this article can be found online at https://doi.org/10.1016/j.mtsust.2023.100334.

References

[1] S.K. Kirthink, S.K. Singh, A. Chourasia, Alternative fine aggregates in production of sustainable concrete – a review, J. Clean. Prod. 268 (2020), 122089.
[2] J. Solé, et al., Modelling the renewable transition: scenarios and pathways for a decarbonized future using pymedeas, a new open-source energy systems model, Renew. Sustain. Energy Rev. 132 (2020), 110105.
[3] A.A. Sakharova, P.A. Sidyakin, D.M. Shchitov, A.V. Nesterchuk, Recyclying of waste to secondary raw materials as a way to increase environmental safety of production, IOP. Conf. Series. 913 (2020), 052066.
[4] A. Irastorza, I. Zarandona, M. Andonegi, P. Guerrero, K. de la Caba, The versatility of collagen and chitosan: from food to biomedical applications, Food Hydrocolloids 116 (2021), 106633.
[5] A. Stanzione, A. Polini, V. La Pesa, A. Quattrini, A. Romano, G. Gigli, L. Moroni, F. Gervaso, Thermosensitive chiotosan-based hydrpgels supporting motor neuron-like NSC-34 cell differentiation, Biomater. Sci. 9 (2021) 7492–7503.
[6] A.L. Oliveira, M. von Staszewski, V.M. Pizones Ruiz-Henestrosa, M. Pintado, A.M.R. Pilosof, Impact of pectin or chitosan on bulk, interfacial and antioxidant properties of (+)-catechin and β-lactoglobulin ternary mixtures, Food Hydrocolloids 55 (2016) 119–127.
[7] A. Piotrowska-Kirschling, K. Szelagowska-Rudzka, J. Karczewski, J. Brzeska, Application of shrimp waste for the synthesis of polyurethane-chitosan materials with potential use in soprtion of oil micro-spills in water treatment, Sustain. Times 13 (2021) 5098.
[8] F. Scalera, F. Gervaso, K.P. Sanosh, A. Sannino, A. Licciulli, Influence of the calcination temperature on morphological and mechanical properties of highly porous hydroxyapatite scaffolds, Ceram. Int. 39 (2013) 4839–4846.
[9] J. Ramírez-Rico, J. Martínez-Fernandez, M. Singh, Biomorphic ceramics from wood-derived templates, Int. Mater. Rev. 62 (2017) 465–485.
[10] R.C. Pullar, P. Marques, J. Amaral, J.A. Labrincha, Magnetic wood-based biomorphic $Sr_3Co_2Fe_{24}O_{41}$ Z-type hexaferrite ecoceramics made from cork templates, Mater. Des. 82 (2015) 297–303.
[11] F. Scalera, L. Carbone, S. Bettini, R.C. Pullar, C. Piccirillo, Biomimetic calcium carbonate with hierarchical porosity produced using cork as sustainable template agent, J. Environ. Chem. Eng. 8 (2020), 103594.
[12] F. Scalera, A. Quarta, D.M. Tobaldi, R.C. Pullar, C. Piccirillo, Cork-derived hierarchically porous hydroxyapatite with different stoichiometries for biomedical and environmental applications, Mater. Chem. Front. 5 (2021) 5071–5081.
[13] A. Polini, D. Pisignano, M. Parodi, R. Quarta, S. Scaglione, Osteoinduction of human mesenchymal stem cells by bioactive composite scaffolds without supplemental osteogenic growth factor, PLoS One 6 (2011), e26211.
[14] S.V. Dorozhkin, Calcium orthophosphate-based bioceramics, Mater 6 (2013) 3840–3942.
[15] A.A. Vu, S.F. Robertson, D. Ke, A. Bandyopadhyay, S. Bose, Mechaical and biological properties of ZnO, SiO_2, and Ag_2O doped plasma sprayed hydroxyapatite coating for orthopedic and dental applications, Acta Biomater. 92 (2019) 325–335.
[16] L. Pighinelli, M. Kucharska, Chitosan-hydroxyapatite composites 93 (2013) 256–262.
[17] B. Li, et al., Biological and antibacterial properties of the micro-nanostrctured hydroxyapatite/chitosan coating on titanium, Sci. Rep. 9 (2019), 14052.
[18] S. Banejee, et al., Antimicrobial and biocompatible fluorescent hydroxyapatite-chitosan nanocomposite film for biomedical applications, Colloids Surf., B 171 (2018) 300–307.
[19] X. Du, M. Dehghani, N. Alsaadi, M.G. Nejad, S. Saber-Samandari, D. Toghraie, C.H. Su, H.C. Nguyen, A Femoral shape porous scaffold bio-nanocomposite fabricated using 3D printing and freeze-drying technique for orthopedic application, Mater. Chem. Phys. 275 (2022), 125302.
[20] D. Boudemagh, P. Venturini, S. Fleutot, F. Cleymand, Elaboration of hydroxyapatite and chitosan/hydroxyapatite composites: a present status, Polym. Bull. 76 (2019) 2621–2653.
[21] P. Scardi, M. Leoni, Whole powder pattern modelling, Acta Crystallogr. A 58 (2002) 190–200.
[22] M. Leoni, T. Confente, P. Scardi, PM2K: a flexible program implementing whole powder pattern modelling, Zeit. Krist. Suppl. 23 (2006) 249–254.
[23] P. Scardi, M. Leoni, Whole powder pattern modelling: theory and Applications, in: Diffraction Analysis of the Microstructure of the Materials”, Springer Series in Materials Science, 2004.
[24] G. Caglioti, A. Paoletti, F.P. Ricci, On resolution and luminosity of a neutron diffraction spectrometer for single crystal analysis, Nucl. Instrum. Methods 9 (1960) 195–198.
[25] A. Lertwosasirikul, S. Yokoyama, K. Noguchi, K. Ogawa, K. Okuyama, Molecular and crystal structures of chitosan/HI type I salt determined by X-ray fiber diffraction, Carbohydr. Res. 339 (2004) 825–833.
[26] A. Bucciarelli, T. Muthukumar, J.S. Kim, W.K. Kim, A. Quaranta, D. Maniglio, G. Khang, A. Motta, Preparation and statistical characterization of tunable

porous sponge scaffolds using UV cross-linking of methacrylate-modified silk fibroin, ACS Biomater. Sci. Eng. 5 (2019) 6374–6388.
[27] C.S. Cunha, P.J. Castro, S.C. Sousa, R.C. Pullar, D.M. Tobaldi, C. Piccirillo, M.M. Pintado, Films of chitosan and natural modified hydroxyaypatite as effective UV-protecting, biocompativle and antibacterial wound dressing, Int. J. Biol. Macromol. 159 (2020) 1177–1185.
[28] A. Ressler, J. Ródenas-Rochina, M. Ivanković, H. Ivanković, A. Rogina, G.G. Ferrer, Injectable chitosan-hydroxyapatite hydrogles promote the osteogenic differentiation of mesenchymal stem cells, Carbohydr. Polym. 197 (2018) 469–477.
[29] F. Scalera, A.G. Monteduro, G. Maruccio, L. Blasi, F. Gervaso, E. Mazzotta, C. Malitesta, C. Piccirillo, Sustainable chitosan-based electrical responsive scaffolds for tissue engineering applications, Sust. Mater. Tech. 28 (2021), e00260.
[30] M.A. Nazeer, E. Yilgör, I. Yilgör, Intercalated chitosan/hydroxyapatite nanocomposites; Promising materials for bone tissue engineering, Carbohydr. Polym. 175 (2017) 38–46.
[31] A. Shavandi, A.E.A. Bekhit, M.A. Ali, Z. Sunm, Bio-mimetic composite scaffold from mussell shells, squid pen and crab chitosan for bone tissue engineering, Int. J. Biol. Macromol. 80 (2015) 445–454.
[32] S. Scialla, et al., Mussel shell-derived macroporous 3D scaffold: characterization and optimization study of a bioceramic from the circular economy, Mar. Drugs 18 (2020) 309.
[33] N.M. Julkapli, Z. Ahmad, H.M. Akil, X-Ray Diffraction studies of cross linked chitosan with different cross linking agents for waste water treatment application, AIP Conf. Proc. 1202 (2010) 106–111.
[34] M. Eddya, B. Tbib, K. EL-Hami, A comparison of chitosan properties after extraction from shrimps shells by diluted and concentrated acids, Helyion 6 (2020), e03489.
[35] C. Qiao, X. Ma, J. Zhang, J. Yao, Molecular interactions in gelatin/chitosan composite films, Food Chem. 235 (2017) 45–50.
[36] W. Tachaboonyakiat, T. Serizawa, M. Akashi, Hydroxyapatite formation on/in biodegradable chitosan hydrogels by an alternate soaking process, Pol. J. 33 (2001) 177–181.
[37] P. Kanokpreechawut, et al., Incorporation of chitosan whisker and hydroxyapatite: a synergistic approach to reinforce chitosan/poly(ethylene glycol) gel, Polym. Degrad. Stabil. 164 (2019) 198–205.
[38] E.A. Syukkalova, A.V. Sadetskaya, N.D. Demidova, N.P. Bobrysheya, M.G. Osmolowsky, M.A. Voznesenskiy, O.M. Osmolovskaya, The effect of the reaction medium and hydrothermal synthesis conditions on morphological parameters and thermal behavior of calcium phosphate nanoparticles, Ceram. Int. 47 (2021) 2809–2821.
[39] S.C. Cox, P. Jamshidi, L.M. Grover, K.K. Mallick, Low temperature aqueous precipitation of needle-like nanophase hydroxyapatite, J. Mater. Sci. Mater. Med. 25 (2014) 37–46.
[40] Y.P. Guo, J.J. Guan, J. Yang, Y. Wang, C.Q. Zhang, Q.F. Ke, Hybrid nanostructured hydroxyapatite/chitosan composite scaffold: bioinspired fabrication, mechanical property and biological property 3 (2015) 4679–4689.
[41] N. Parekh, C. Hushye, S. Warunkar, S.S. Gupta, A. Nisal, *In vitro* study of novel microparticle based silk fibroin scaffold with osteoblast-like cells for load-bearing osteo-regenerative applications, RSC Adv. 7 (2017) 26551–26558.
[42] H. Park, M.H. Kim, Y.I. Yoon, W.H. Park, One-pot synthesis of injectable methylcellulose hydrogel containing calcium phosphate nanoparticles, Carbohydr. Polym. 157 (2017) 775–783.
[43] M.H. Kim, H. Park, W.H. Park, Effect of pH and precursor salts on in situ formation of calcium phosphate nanoparticles in methylcellulose hydrogels, Carbohydr. Polym. 191 (2018) 176–182.
[44] A. Rogina, A. Ressler, I. Matić, G. Gallego Ferrer, I. Marijanović, M. Ivanković, H. Ivanković, Cellular hydrogels based on pH-responsive chitosan-hydroxyapatite system, Carbohydr. Polym. 166 (2017) 173–182.
[45] C.N. Costa, V.G. Teixeira, M.C. Delpech, J.V.S. Souza, Viscometric study of chitosan solutions in acetic acid/sodium acetate and acetic acid/sodium chloride, Carbohydr. Polym. 133 (2015) 245–250.
[46] P. Chen, L. Liu, J. Pan, J. Mei, C. Li, Y. Zheng, Biomimetic composite scaffold of hydroxypatite/gelatine-chitosan core-shell nanofibers for bone tissue engineering, Mater. Sci. Eng. C 97 (2019) 325–335.
[47] V. Perez-Puyana, J.F. Rubio-Vale, M. Jiménez-Rosado, A. Guerrero, A. Romero, Alternative processing methods of hybrid porous scaffolds based on gelatin and chitosan, J. Mech. Behav. Biomed. Mater. 102 (2020), 103472.
[48] F. Gervaso, F. Scalera, K.P. Sanosh, A. Licciulli, D. Deponti, A. Di Giancamillo, C. Domeneghini, G.M. Peretti, A. Sannino, Development and Mechanical Characterization of a Collagen/Hydroxyapatite Bilayered Scaffold for Osteochondral Defect Replacement, vols. 493–494, 2012, pp. 890–895.
[49] S. Been, J. Choi, H. Cho, G. Jeon, J.E. Song, A. Bucciarelli G. Khang, Preparation and characterization of a soluble eggshell membrane/agarose composite scaffold with possible applications in cartilage regeneration, J Tissue Eng Regen Med 15 (2021) 375–387.
[50] L.L. Fernandes, C.X. Resende, D.S. Tavares, G.A. Soares, Cytocompatibility of chitosan and collagen-chitosan scaffolds for tissue engineering, Polimery 21 (2011) 1–6.
[51] M.A. Rebelo, M. Chaud, V.M. Balcão, M.D.C. Vila, N. Aranha, V.M.H. Yoshida, T.F. Alves, J.M. Oliveira Jr., Chitosan-based scaffolds for tissue regeneration: preparation and microstructure characterization, ejbps 3 (2016) 15–24.
[52] D. Izzo, B. Palazzo, F. Scalera, F. Gullotta, V. Iapesa, S. Scialla, A. Sannino, F. Gervaso, Chitosan scaffolds for cartilage regenration: influence of different ionic crosslinkers on biomaterial properties, Int. J. Polym. Mater. Polym. Biomater. 68 (2019) 936–945.
[53] B. Qasim, S. Husain, Y. Huang, M. Pogorielov, V. Deineka, M. Lyndin, A. Rawlinson, I.U. Rehman, In-vitro and in-vivo degradation studies of freeze gelated porous chitosan composite scaffolds for tissue engineering applications, Polym. Degrad. Stabil. 136 (2017) 31–38.
[54] W. Wang, C. Xue, X. Mao, Chitosan: structural modification, biological activity and application, Int. J. Biol. Macromol. 164 (2020) 4532–4546.
[55] M. Wang, S. Bi, D. Qin, C. Su, H. Wang, X. Chen, Quantitative evaluation of the antibacterial effectiveness and efficiency of chitosan considering the effect of neutralization, Carbohydr. Polym. 265 (2021), 117918.
[56] J. Li, J. Fu, X. Tian, T. Hua, T. Poon, M. Koo, W. Chan, Characteristics of chitosan fiber and their effects towards improvement of antibacterial activity, Carbohydr. Polym. 280 (2022), 119031.
[57] M.A. Matica, F.L. Aachmann, A. Tøndervik, H. Sletta, V. Ostafe, Chitosan as a wound dressing starting material: antimicrobial properties and mode of action, Int. J. Mol. Sci. 20 (2019) 5889–5921.